Switching of charge-density wave by carrier tuning in monolayer $TiTe_2$

Koki Yanagizawa,[1] Katsuaki Sugawara,[1,2,3] Tappei Kawakami,[1] Ryuichi Ando,[1] Ken Yaegashi,[1] Kosuke Nakayama,[1] Seigo Souma,[2,4] Kiyohisa Tanaka,[5] Miho Kitamura,[6] Koji Horiba,[7] Hiroshi Kumigashira,[8] Takashi Takahashi,[1] and Takafumi Sato[1,2,4,9,10]

[1]*Department of Physics, Graduate School of Science, Tohoku University, Sendai 980-8578, Japan*
[2]*Advanced Institute for Materials Research (WPI-AIMR), Tohoku University, Sendai 980-8577, Japan*
[3]*Precursory Research for Embryonic Science and Technology (PRESTO), Japan Science and Technology Agency (JST), Tokyo 102-0076, Japan*
[4]*Center for Science and Innovation in Spintronics (CSIS), Tohoku University, Sendai 980-8577, Japan*
[5]*UVSOR Synchrotron Facility, Institute for Molecular Science, Okazaki 444-8585, Japan*
[6]*Photon Factory, Institute of Materials Structure Science, High Energy Accelerator Research Organization (KEK), Tsukuba 305-0801, Japan*
[7]*National Institutes for Quantum Science and Technology (QST), Sendai 980-8579, Japan*
[8]*Institute of Multidisciplinary Research for Advanced Materials (IMRAM), Tohoku University, Sendai 980-8577, Japan*
[9]*International Center for Synchrotron Radiation Innovation Smart (SRIS), Tohoku University, Sendai 980-8577, Japan*
[10]*Mathematical Science Center for Co-creative Society (MathCCS), Tohoku University, Sendai 980-8578, Japan*

(Received 2 May 2023; accepted 25 September 2023; published 18 October 2023)

How charge-density wave (CDW) is influenced by the change in the dimensionality is a fundamental question in condensed-matter physics. Monolayer titanium ditelluride ($TiTe_2$) undergoes 2×2 CDW despite the absence of CDW in the bulk counterpart, whereas the mechanism of CDW is under intensive debate. Here we show that the CDW of monolayer $TiTe_2$ can be conveniently switched by carrier tuning via controlling the Te ratio during molecular-beam epitaxy or depositing potassium (K) atoms on the surface. This is demonstrated by monitoring the CDW-induced 2×2 band folding using angle-resolved photoemission spectroscopy. Remarkably, the CDW appears only when the inner hole pocket at the Γ point and the elongated electron pocket at the M point show partial Fermi-surface nesting. The present study suggests that the carrier doping is an effective method to pin down the mechanism of CDW in atomic-layer transition-metal dichalcogenides.

DOI: 10.1103/PhysRevMaterials.7.104002

I. INTRODUCTION

Initiated by the discovery of a massless Dirac fermion in graphene and associated quantum phenomena such as half integer quantum Hall effect and valley Hall effect [1,2], a search for new two-dimensional (2D) materials hosting exotic physical properties is now becoming one of the central topics in material science. Transition-metal dichalcogenides (TMDs) offer an excellent platform to realize new 2D materials, not only because bulk TMDs already show outstanding physical properties such as superconductivity, charge-/spin-density wave (CDW/SDW), magnetic order [3], and exotic topological phases [4–6], but also because its layered structure is suitable to study the evolution of electronic states from the bulk to the thinnest monolayer limit. Perhaps CDW is a most fundamental and longstanding issue in the bulk and ultrathin TMDs because many TMDs undergo CDW with a variety of lattice periodicities, essentially due to the low-dimensional (2D or quasi-2D) nature of electronic states which enhances the electronic instability toward the CDW transition. Also, since the CDW phase often appears in or close to other quantum phases such as Mott-insulator [7,8], superconductivity [9], and magnetic phases [10,11], its interplay (such as competition and coexistence) has been fiercely debated.

Titanium ditelluride ($TiTe_2$) with octahedral ($1T$-) structure is an excellent platform to study the interplay between CDW and dimensionality, because it was reported to show intriguing differences in the CDW properties between bulk and monolayer. Bulk $TiTe_2$ is a simple semimetal [12] characterized by the compensated quasi-2D hole pockets at the Γ/A point and a strongly warped quasi-2D electron pocket at the L point of the bulk Brillouin zone (BZ) [13,14] and it does not exhibit CDW. On the other hand, the monolayer counterpart [see Fig. 1(a) for the crystal structure] was recently reported to show CDW accompanied by 2×2 superstructure. This periodicity is identical to that observed in isostructural monolayer $TiSe_2$ in which the CDW phase is proposed to be stabilized by the condensation of excitons [15] as in the case of bulk $TiSe_2$ showing similar $2 \times 2 \times 2$ CDW [16–20]. Thus the contrasting CDW behavior between bulk and monolayer is a peculiar characteristic of $TiTe_2$. To account for this unusual CDW, previous ARPES studies have proposed several key ingredients such as electron-phonon coupling and orbital selective hybridization [14,21], although the mechanism of CDW is still unclear. Examination of the Fermi surface (FS) nesting condition via controlling the carrier concentration is useful to pin down the origin of CDW, whereas such studies have not been reported in monolayer $TiTe_2$.

In this article, we report angle-resolved photoemission spectroscopy (ARPES) investigation of monolayer $TiTe_2$ on bilayer graphene grown by the molecular-beam epitaxy (MBE) method. By controlling the annealing temperature

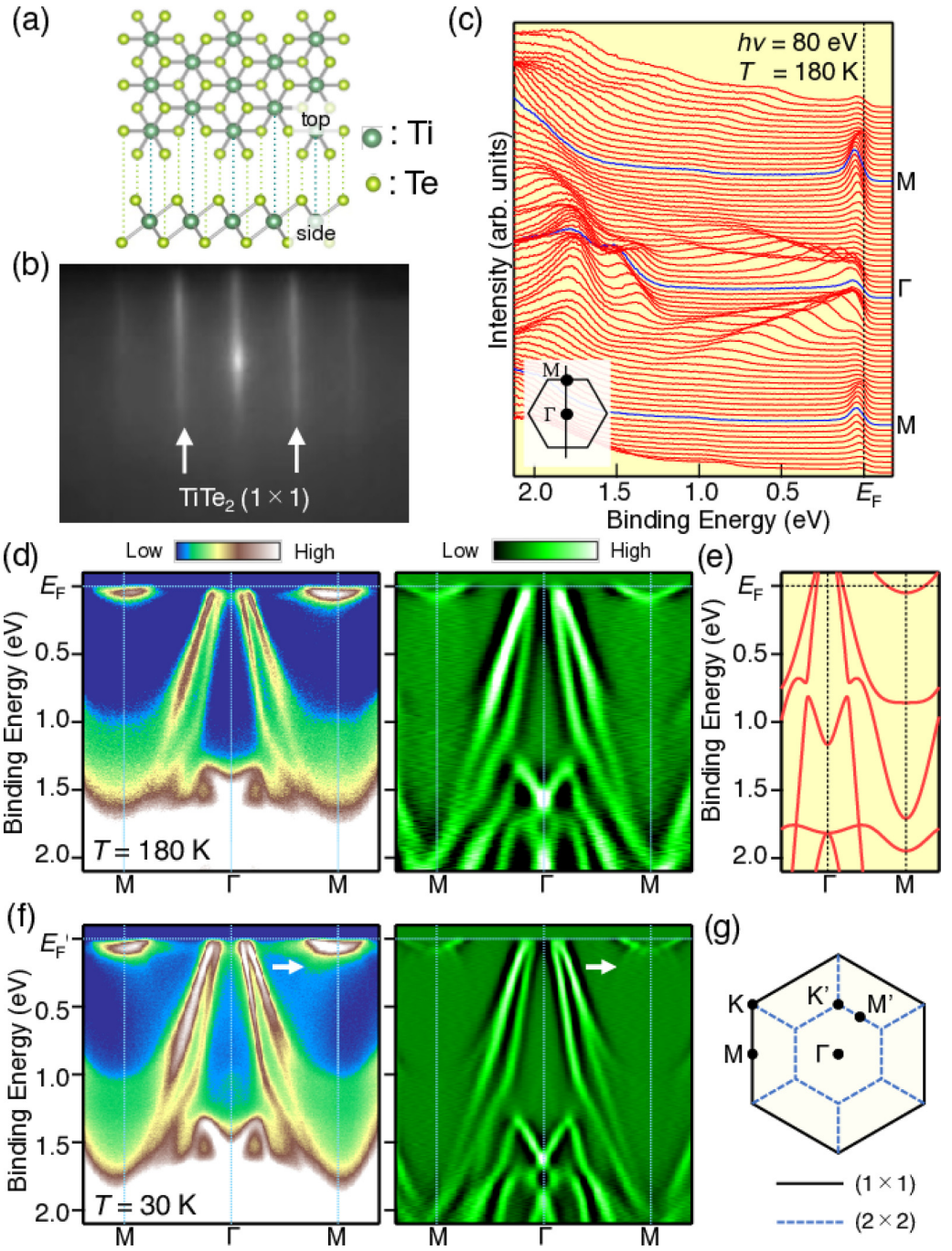

FIG. 1. (a) Schematic view of crystal structure of monolayer $1T-TiTe_2$. (b) RHEED pattern of $TiTe_2$ grown on bilayer graphene/SiC. Electron beam is incident along the $[1\bar{1}00]$ direction of the SiC substrate. (c) EDCs of monolayer $1T-TiTe_2$ measured along the $M\Gamma M$ cut at $T = 180$ K with $h\nu = 80$ eV. (d) (Left) Plots of ARPES intensity and (right) corresponding second-derivative intensity of monolayer $1T-TiTe_2$ along the $M\Gamma M$ cut at $T = 180$ K. (e) Calculated band structure of monolayer $1T-TiTe_2$ obtained with the first-principles band calculations. (f) Same as (d) but measured at $T = 30$ K. White arrows highlight folded bands associated with the formation of 2×2 CDW. (g) BZ of $1T-TiTe_2$ in the normal phase (black solid line) and the 2×2 CDW phase (blue broken line).

during epitaxy or depositing K atoms on the surface, we have succeeded in systematically controlling the carrier concentration in a wide doping range from a slightly hole-doped to a heavily electron-doped region. As a consequence, we found that the 2×2 CDW appears only in a very narrow doping range in which the electron and hole carriers are compensated. We discuss the implications of the present results in relation to the fermiology and various CDW mechanisms such as FS nesting and exciton condensation, by also comparing the band structure with isostructural $TiSe_2$.

II. EXPERIMENTS AND CALCULATIONS

A. Sample fabrication

The high-quality monolayer $TiTe_2$ film was grown on bilayer graphene by the MBE method [7,8,15]. First, bilayer

graphene was fabricated by resistive heating of n-type 4H-SiC(0001) single-crystal wafer at 1100 °C for 30 min under high vacuum better than 1.0×10^{-9} Torr. Subsequently, a monolayer $TiTe_2$ film was grown by evaporating Ti atoms on the bilayer graphene substrate kept at 400–440 °C in the Te-rich atmosphere and then the as-grown monolayer $TiTe_2$ film was annealed for 30 min at 400 °C. The growth process was monitored by the reflection high-energy electron diffraction (RHEED). After the growth, the film was transferred to the ARPES measurement chamber without exposing it to air. As seen in Fig. 1(b), the RHEED pattern for the $TiTe_2$ film shows a sharp 1×1 streak pattern, confirming the high crystallinity of film.

B. ARPES measurements

ARPES measurements were carried out using a DA-30 electron energy analyzer with a microfocused synchrotron-radiation at the beamline BL-28A of Photon Factory (KEK) [22] and a MBS A1 electron energy analyzer at the beamline BL5U in UVSOR. The energy and angular resolutions were set to be 25–50 meV and 0.2–0.3°, respectively. The Fermi level (E_F) of the sample was calibrated with a gold film deposited onto the substrate. The potassium (K) deposition was carried out using a K dispenser (SAES Getters) in a vacuum of $\sim 1.0 \times 10^{-9}$ Torr.

C. Band-structure calculations

First-principles band-structure calculations were carried out by using the QUANTUM-ESPRESSO package [23,24] with generalized gradient approximation [25]. The plane-wave cut-off energy and uniform k-point mesh were set to be 60 Ry and $12 \times 12 \times 1$, respectively. The thickness of the inserted vacuum layer was set to be more than 10 Å to prevent interlayer interaction.

III. RESULTS AND DISCUSSION

A. Electronic structure of monolayer $TiTe_2$

First we present the electronic states of pristine monolayer $TiTe_2$. Figure 1(c) shows energy distribution curves (EDCs) in the valence-band region measured along the ΓM cut of the hexagonal BZ at $T = 180$ K above the CDW transition temperature ($T_{CDW} \sim 90$ K). One can recognize a couple of hole bands crossing E_F centered at the Γ point and a shallow electron band in the vicinity of E_F centered at the M point, which are assigned to the Te $5p$ and Ti $3d$ orbitals, respectively [13,14]. Corresponding ARPES-intensity and second-derivative plots shown in Fig. 1(d) signify an M-shaped band around the Γ point at $\sim$1.5 eV besides the Γ-centered hole and M-centered electron bands, in reasonable agreement with the calculated band structure of monolayer $1T-TiTe_2$ shown in Fig. 1(e). These results indicate that pristine monolayer $TiTe_2$ is a compensated semimetal with a negative band gap, consistent with the previous studies [13,14]. As shown in the left panel of Fig. 1(f), the overall ARPES intensity at $T = 30$ K appears to be similar to that at $T = 180$ K. On the other hand, there exists an extra intensity below the electron band at the M point at $T = 30$ K as indicated by a white arrow. Such an extra intensity is completely absent at $T = 180$ K. As seen from the second derivative intensity plot in the right panel of Fig. 1(f), this extra feature is the replica of the two hole bands at the Γ point which are folded to the M point due to the 2×2 periodic potential of CDW [14,21,27], as also clearly seen from the momentum distribution curves (MDCs) around the M point (see Fig. S1 in the Supplemental Material [26]). Moreover, by following the periodicity of reconstructed BZ [see the original and reconstructed BZs in Fig. 1(g)], the shallow electron band at the M point is folded back to the Γ point (see Fig. S2 in Supplemental Material [26]). These results strongly suggest that the electronic structure at $T = 30$ K is reconstructed by the formation of 2×2 CDW, consistent with the previous reports [14,21,27]. We estimated the intensity ratio of folded hole bands around the M point relative to that of the main hole bands around the Γ point to be $\sim$10%, which is distinct from the case of $T = 180$ K in which the intensity ratio is 0% because of the complete absence of the folded hole bands. It is also noted that the spectral weight of folded bands is much weaker than that of isostructural monolayer $TiSe_2$ (and also bulk $TiSe_2$) [15,18,19,28,29]. We will come back to this point later.

B. Carrier doping effect on the CDW

Next, we present how the CDW is influenced by the change in the carrier concentration. While the previous studies have focused on the experiments on the pristine sample, we are able to modulate the carrier concentration by adopting two methods, i.e., (i) changing the substrate temperature T_s during the epitaxy to effectively control the stoichiometry of the sample and (ii) systematically depositing potassium (K) atoms on pristine $TiTe_2$. Figures 2(a)–2(c) show (top panel) ARPES intensity and (bottom panel) corresponding second derivative intensity plots along the ΓM cut, measured at $T = 40$ K, for three different T_s values of 400, 420, and 440 °C, respectively; note that the data for $T_s = 420$ °C were already presented in Fig. 1. One can recognize a systematic change in the band structure upon increasing T_s. For example, the bottom of the electron band at the M point systematically moves downward to cause the expansion of the electron pocket. Also, $\mathbf{k}_F$ points of the hole bands move toward the Γ point, being associated with the shrinkage of the hole pockets. These changes are more clearly visualized in the ARPES intensity at E_F plotted as a function of a 2D wave vector in Figs. 2(d)–2(f). From the size of electron and hole pockets in the FS mapping (see red circles and dashed black curves), we have estimated the electron and hole carrier concentrations for the $T_s = 420$ °C sample to be $\sim 0.08e^-$ and $\sim 0.08h^+$, respectively (for details to estimate the carrier concentration, see Supplemental Material S3 [26]). This suggests the effectively zero total carriers and the well compensated nature. Thus one can define this sample as a "pristine" sample. On the other hand, we have estimated the total carrier for the $T_s = 400$ °C and 440 °C samples to be $\sim 0.06h^+$ and $\sim 0.37e^-$, respectively, indicative of the violation of the compensated nature. These results suggest that the tuning of T_s works as an effective method to control the carrier concentration. We speculate that the annealing at slightly higher temperature than

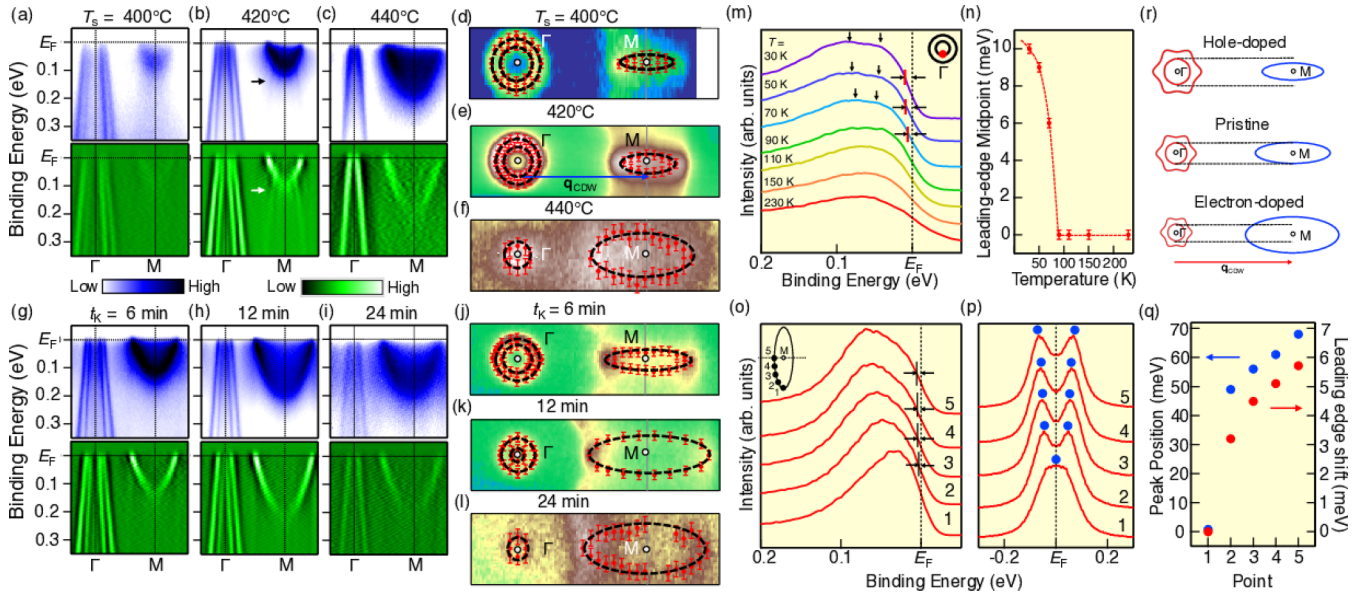

FIG. 2. (a)–(c) (Top) Plots of ARPES intensity and (bottom) corresponding second-derivative intensity along the $M\Gamma M$ cut for monolayer $TiTe_2$ grown at the substrate temperature of $T_s = 400$, 420, and 440 °C, respectively. (d)–(f) Plots of ARPES intensity as a function of 2D wave vector integrated within an energy window of $E_F \pm 50$ meV for the films shown in (a)–(c). Blue arrow in (e) corresponds to the 2×2 nesting vector $\mathbf{q}_{CDW}$. Red circles are $\mathbf{k}_F$ points determined by tracing the band dispersion and black curves are experimental FS determined from the estimated $\mathbf{k}_F$ points. (g)–(i) K-dosing dependence of the ARPES intensity and corresponding second-derivative plots for the K dosing time of $t_K = 6$, 12, and 24 min, respectively. (j)–(l) Same as (d)–(f) but for the films shown in (g)–(i). (m) Temperature dependence of EDC measured at the $\mathbf{k}_F$ point of the inner hole pocket shown in the inset (red circle). (n) Plot of leading-edge shift as a function of temperature which signifies T_{CDW} of ∼90 K. (o) EDCs at $T = 30$ K on the ellipsoidal electron pocket at the M point obtained at representative $\mathbf{k}_F$ points (points 1–5) shown in the inset. (p) Corresponding symmetrized EDCs. Peak position is indicated by blue circles. (q) Plot of leading-edge shift (red circles) in the EDCs and peak position in symmetrized EDCs (blue circles) at five representative $\mathbf{k}_F$ points (points 1–5). (r) Schematic FS topology for hole-doped, pristine, and electron-doped monolayer $TiTe_2$. Horizontal dashed lines represent the size of the inner hole pocket. $\mathbf{q}_{CDW}$ is also shown by red arrow.

the optimal value of $T_s = 420$ °C produces Te deficiencies in the film that work as an electron donor. On the other hand, annealing at a slightly lower temperature than the optimal one creates Te adatoms on the film that work as an effective accepter probably due to the slightly larger work function of Te (4.95 eV) [30] than that of $TiTe_2$ (4.86 eV) [31].

Interesting physics manifests itself when we carefully monitor the folded bands at the M point. While the $T_s = 420$ °C sample apparently shows replica hole bands at the M point due to CDW [arrows in the top and bottom panels of Fig. 2(b)], the replica bands are not seen for both the $T_s = 400$ °C [Fig. 2(a)] and 440 °C [Fig. 2(c)] samples. This suggests that CDW appears only in a narrow carrier concentration range around the zero total carrier in both the hole- and electron-doped regions. To further examine the evolution of band structure upon carrier doping, we have systematically deposited K atoms on the pristine sample ($T_s = 420$ °C) and show in Figs. 2(g)–2(i) the ARPES intensity for the K dosing time t_K of 6, 12, and 24 min. It is evident that the dosing of K atoms systematically moves the electron and hole bands downward indicative of electron doping into the system, similarly to the case of increasing T_s. The effective total carrier estimated from the FS volume shown in Figs. 2(j)–2(l) is $\sim 0.07e^-$, $\sim 0.21e^-$, and $\sim 0.39e^-$ for $t_K = 6$, 12, and 24 min, respectively. These values correspond to the effective K coverage of 7, 21, and 39% per $TiTe_2$ unit cell, under the assumption that one K atom donates one electron to a $TiTe_2$ layer. As can be seen from Figs. 2(g)–2(i), folded bands are always absent irrespective of t_K. This suggests that CDW appears only at the zero doping where electron and hole carriers are compensated.

C. Observation of a CDW gap

To clarify the CDW transition temperature (T_{CDW}) in monolayer $TiTe_2$, we have performed the temperature-dependent ARPES measurements near E_F. Figure 2(m) shows the EDCs at the $\mathbf{k}_F$ point on the inner hole pocket around the Γ point measured at various temperatures ($T = 30$–230 K). One can see that the leading-edge midpoint is shifted toward higher E_B by 2–10 meV at $T = 30$ K, accompanied by a two-peaked structure (black arrows). The peak closer to E_F is associated with the CDW-gap opening, whereas that at higher E_B is produced by the electron band folded from the M point due to the 2×2 CDW formation [21]. On increasing temperature, the leading-edge midpoint gradually moves toward E_F and finally reaches E_F at $T = 90$ K, suggesting that the CDW sets in at ∼90 K. We found that the CDW gap opens also on the electron pocket at the M point and it is strongly anisotropic. As seen from Fig. 2(o), there is a peak at 70 meV in the EDC at the $\mathbf{k}_F$ point along the shorter axis of the ellipsoidal pocket (point 5 in the inset) where the FS of the ellipsoidal pocket overlaps well with the folded inner hole pocket. This peak exhibits a finite leading-edge shift toward higher E_B (see vertical black line

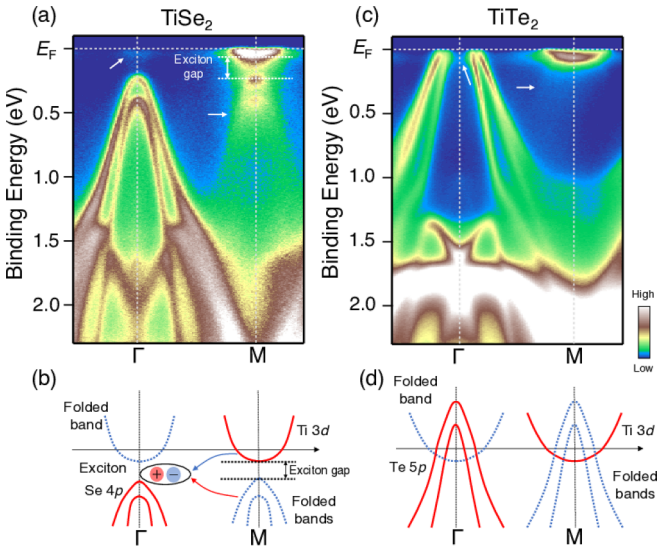

FIG. 3. (a) ARPES-intensity plots of monolayer $TiSe_2$ measured along the ΓM cut in the CDW phase. (b) Schematics of the overall band structure for monolayer $TiSe_2$. (c), (d) Same as (a) and (b) but for monolayer $TiTe_2$.

and arrows) due to the CDW-gap opening. On approaching the longer axis of the ellipsoidal pocket (from point 5 to point 1), the peak systematically approaches E_F and the leading-edge shift eventually vanishes. This strong **k** dependence is better visualized in the symmetrized EDCs in Fig. 2(p) as well as the plot of peak position in the symmetrized EDCs and leading-edge shift in Fig. 2(q). From the analyses of the FS, we found that the inner hole pocket at Γ and the elongated electron pocket at M partially overlap by the 2×2 **q** vector ($\mathbf{q}_{\mathrm{CDW}}$) in the pristine sample, as schematically shown in Fig. 2(r). We will come back to this point later.

D. Mechanism of CDW

Now that the band structure of pristine and doped monolayer $TiTe_2$ is established, an important question is the mechanism of CDW in monolayer $TiTe_2$, which occurs only in the pristine sample. We compare in Fig. 3 the band structure between monolayer $TiTe_2$ and isostructural monolayer $TiSe_2$ which also undergoes a 2×2 CDW below ~240 K [15,28,29,32]. In the CDW phase of monolayer $TiSe_2$ [Fig. 3(a)], replica hole bands with a sizable intensity at the M point associated with the exciton condensation are seen, in line with its indirect zero-gap semiconducting nature which does not satisfy the FS-nesting condition [15]. The exciton condensation is associated with the strong Coulomb interaction between electron and hole [Fig. 3(b)] [16–20] and gives rise to a sizable energy gap (exciton gap) of ~0.2 eV [18–20]. On the other hand, monolayer $TiTe_2$ is a semimetal with a negative band gap [Fig. 3(c)] so that it is hard to stabilize excitons because of the strong screening by mobile carriers [Fig. 3(d)]. Thus the exciton condensation mechanism is unlikely to account for the observed 2×2 CDW in monolayer $TiTe_2$ as discussed in the previous studies [13,14].

There are some other mechanisms to possibly account for the CDW in $TiTe_2$, such as (i) disorder effect, (ii) electron scattering between van Hove singularities [33–35], (iii) the Jahn-Teller distortion [36], (iv) strong electron-phonon coupling [37–40], and (v) FS nesting. Scenario (i) is unlikely because we observed that the quasiparticle lifetime remains unchanged even in the K-deposited ($t_K = 6$ min) sample in which the CDW is absent (see Fig. S5 in the Supplemental Material [26]). Scenario (ii) is also ruled out because the band structure in the normal state does not contain van Hove singularities. For scenario (iii), the Jahn-Teller distortion is generally accompanied by the change in the atomic arrangement and the crystal symmetry, leading to the energy shift of bands, band folding, and sometimes lifting of band degeneracy. We found that the energy position of bands (such as the M-shaped band at 1.6–2.0 eV at the Γ point, two hole bands dispersing toward E_F around the Γ point, and the electron band at the M point) shows no apparent difference between $T = 180$ K and 30 K [Figs. 1(d) and 1(f)] except for the energy-gap opening in the vicinity of E_F. This implies that the influence of Jahn-Teller distortion to the electronic states (if it exists) may be rather small, while a structural experiment to determine the exact amount of distortion needs to be further carried out. For scenario (iv), we found that a kink in the energy dispersion, a hallmark of a strong electron-phonon coupling, is not clearly observed in monolayer, in contrast to the case of bulk $TiTe_2$ [40] (see Fig. S4 in the Supplemental Material [26]). Since the possibility of insufficient energy resolution is not fully excluded at the moment to account for the absence of kink, further examination of this scenario requires higher-resolution ARPES data and the experimental determination of phonon dispersion below and above T_{CDW}. We think that the most plausible scenario is (v) the FS nesting. As shown by the schematic FS topology for three different doping levels (hole-doped, pristine, and electron-doped) in Fig. 2(r), the inner hole and elongated electron pockets are partially nested with each other in the pristine sample. In fact, we identified an energy gap on the hole pocket below ~90 K associated with the CDW gap, as already demonstrated in Fig. 2(m) (note that the gap opening associated with the overlap between the inner hole pocket and the shorter axis of electron pocket is consistent with the proposed orbital-selective band hybridization [14]). Also, the observation of an anisotropic CDW gap on the electron pocket at the M point is well explained in terms of the FS nesting, because the overlap between the folded hole pocket and the ellipsoidal electron pocket becomes gradually small on approaching point 1 from point 5 as seen in Fig. 2(o), in accordance with the closure of the CDW gap. On the other hand, the FS overlap becomes ill defined in the hole- (top panel) and electron-doped (bottom panel) regimes and no clear signature of the CDW gap was observed in these samples. Specifically, in the hole-doped sample, the electron pocket shrinks and the $\mathbf{k}_F$ point along its shorter axis becomes smaller than that of the inner hole pocket. In the heavily electron-doped sample, the electron pocket significantly expands and its $\mathbf{k}_F$ point becomes larger than that of the outer hole pocket. As a result, the FS of the pristine sample accidentally shows a relatively good nesting condition compared to the doped samples. One may wonder by comparing Figs. 2(e) and 2(j) why the CDW is absent in the $t_K = 6$ min sample which seems to still satisfy the partial nesting condition. While the reason is unclear at the

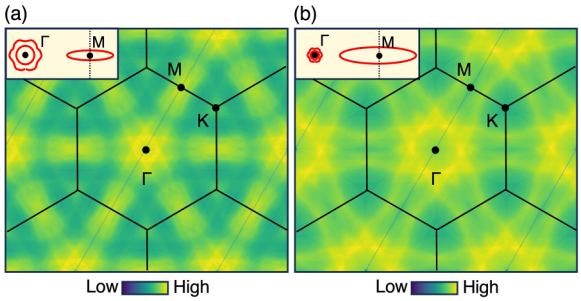

FIG. 4. (a), (b) Intensity plots of Re[$\chi_0(\mathbf{q})$] obtained from the calculated FS for the pristine and electron-doped monolayer $TiTe_2$, respectively. Inset shows the calculated FS. Difference in the chemical potential is 0.1 eV between (a) and (b).

moment, we speculate that the expansion of the longer axis of the ellipsoidal electron pocket in the $t_K = 6$ min sample effectively reduces the ratio of the nested k region with respect to the total FS region, making the CDW relatively unstable. To further examine the scenario of FS-nesting-driven CDW, we calculated the electronic susceptibility $\chi_0(\mathbf{q})$ based on the results of our DFT calculations. Specifically, we calculated the $\mathbf{q}$ (momentum transfer) dependence of the real part of $\chi_0(\mathbf{q})$ (Re[$\chi_0(\mathbf{q})$]), based on the calculated FS for monolayer $TiTe_2$. As seen in Fig. 4(a), a local maximum of Re[$\chi_0(\mathbf{q})$] is located at $\mathbf{q} = 1/2\mathbf{G}$ corresponding to the M point ($\mathbf{G}$: reciprocal lattice vector) in pristine nondoped $TiTe_2$. This feature is associated with the FS nesting between the inner hole pocket and the ellipsoidal electron pocket. On the other hand, in electron-doped $TiTe_2$ (nearly corresponding to the case of $t_K = 12$ min), the bright spot is absent at $\mathbf{q} = 1/2\mathbf{G}$ [Fig. 4(b)], consistent with the absence of the 2×2 CDW in the electron-doped samples. Thus our experimental finding that the FS-nesting-driven CDW is realized only around the nondoped region is supported by the calculated electronic susceptibility. Since appearance/absence of the 2×2 CDW in monolayer $TiTe_2$ is sensitive to the FS topology, it is inferred that the FS-nesting-driven CDW in monolayer $TiTe_2$ is more fragile compared to the exciton-condensation-driven CDW in monolayer $TiSe_2$. The reason why CDW is absent in bulk, but not in monolayer, would be due to the difference in the dimensionality of the FS between bulk and monolayer; i.e., bulk $TiTe_2$ shows a strong warping effect along k_z for the electron pocket at the M/L point which does not favor the FS nesting, instead of the purely 2D pocket in the monolayer case. The high controllability of the FS topology for monolayer $TiTe_2$ established in this study is thereby useful to switch normal metallic and CDW phases. A next step is to search for exotic quantum phases such as superconductivity in the proximity to the CDW phase by perturbing the system using, e.g., electrical gating and/or chemical doping.

IV. CONCLUSION

In conclusion, we performed a high-resolution ARPES study on monolayer $1T-TiTe_2$ grown on bilayer graphene. We have succeeded in controlling the carrier concentration in a wide range, by using two independent methods, controlling the substrate temperature during epitaxy and K dosing on the sample. We found that the 2×2 CDW, as characterized by the band folding, is fragile against carrier doping and emerges only at the effectively zero doping level with the electron and hole compensation. The present study points to importance of carrier tuning to clarify the mechanism of CDW in monolayer TMDs.

ACKNOWLEDGMENTS

This work was supported by JST-CREST (Grant No. JPMJCR18T1), JST-PRESTO (Grant No. JPMJPR20A8), Grant-in-Aid for Scientific Research (JSPS KAKENHI Grants No. JP18H01821, No. JP20H01847, No. JP20H04624, No. JP21H01757, No. JP21K18888, No. JP21H04435, and No. JP22J13724), KEK-PF (Proposals No. 2020G669, No. 2021S2-001, and No. 2022G007), UVSOR (Proposals No. 21-658 and No. 21-679), Foundation for Promotion of Material Science and Technology of Japan, and World Premier International Research Center, Advanced Institute for Materials Research. K. Yanagizawa, T. Kawakami, and K. Yaegashi acknowledge support from GP-Spin at Tohoku University. T. Kawakami also acknowledges support from JSPS.

[1] K. S. Novoselov, A. K. Geim, S. V. Morozov, D. Jiang, M. I. Katsnelson, I. V. Grigorieva, S. V. Dubonos, and A. A. Firsov, Nature (London) **438**, 197 (2005).

[2] R. V. Gorbachev, J. C. W. Song, G. L. Yu, A. V. Kretinin, F. Withers, Y. Cao, A. Mishchenko, I. V. Grigorieva, K. S. Novoselov, L. S. Leviton, and A. K. Geim, Science **346**, 448 (2014).

[3] M. Chhowalla, H. S. Shin, G. Eda, L.-J. Li, K. P. Loh, and H. Zhang, Nat. Chem. **5**, 263 (2013).

[4] X. Qian, J. Liu, L. Fu, and J. Li, Science **346**, 1344 (2014).

[5] Y. Shi, J. Kahn, B. Niu, Z. Fei, B. Sun, X. Cai, B. A. Francisco, D. Wu, Z.-X. Shen, X. Xu, D. H. Cobden, and Y.-T. Cui, Sci. Adv. **5**, eaat8799 (2019).

[6] K. Deng, G. Wan, P. Deng, K. Zhang, S. Ding, E. Wang, M. Yan, H. Huang, H. Zhang, Z. Xu, J. Denlinger, A. Fedorov, H. Yang, W. Duan, H. Yao, Y. Wu, S. Fan, H. Zhang, X. Chen, and S. Zhou, Nat. Phys. **12**, 1105 (2016).

[7] Y. Nakata, K. Sugawara, R. Shimizu, Y. Okada, P. Han, T. Hitosugi, K. Ueno, T. Sato, and T. Takahashi, NPG Asia Mater. **8**, e321 (2016).

[8] Y. Nakata, K. Sugawara, A. Chainani, H. Oka, C. Bao, S. Zhou, P.-Y. Chuang, C.-M. Cheng, T. Kawakami, Y. Saruta, T. Fukumura, S. Zhou, T. Takahashi, and T. Sato, Nat. Commun. **12**, 5873 (2021).

[9] X. Xi, Z. Wang, W. Zhao, J.-H. Park, K. T. Law, H. Berger, L. Forro, J. Shan, and K. F. Mak, Nat. Phys. **12**, 139 (2016).

[10] M. Bonilla, S. Kolekar, Y. Ma, H. C. Diaz, V. Kalappattil, R. Das, T. Eggers, H. R. Gutierrez, M.-H. Phan, and M. Batzill, Nat. Nanotechnol. **13**, 289 (2018).

[11] X. Teng, L. Chen, F. Ye, E. Rosenberg, Z. Liu, J.-X. Yin, Y.-X. Jiang, J. S. Oh, M. Z. Hasan, K. J. Neubauer, B. Gao, Y. Xie, M. Hashimoto, D. Lu, C. Jozwiak, A. Bostwick, E. Rotenberg, R. J. Birgeneau, J.-H. Chu, M. Yi *et al.*, Nature (London) **609**, 490 (2022).

[12] Y. Koike, M. Okamura, T. Nakanomyo, and T. Fukase, J. Phys. Soc. Jpn. **52**, 597 (1983).

[13] S. Beaulieu, M. Schuler, J. Schusser, S. Dong, T. Pincelli, J. Maklar, A. Neef, F. Reinert, M. Wolf, L. Rettig, J. Minar, and R. Ernstorfer, npj Quantum Mater. **6**, 93 (2021).

[14] T. Antonelli, W. Rahim, M. D. Watson, A. Rajan, O, J. Clark, A. Danilenko, K. Underwood, I. Marković, E. Abarca-Morales, S. R. Kavanagh, P. L. Fèvre, F. Bertran, K. Rossnagel, D. O. Scanlon, and P. D. C. King, npj Quant. Mater. **7**, 98 (2022).

[15] K. Sugawara, Y. Nakata, R. Shimizu, P. Han, T. Hitosugi, T. Sato, and T. Takahashi, ACS Nano **10**, 1341 (2016).

[16] D. Jerome, T. M. Rice, and W. Kohn, Phys. Rev. **158**, 462 (1967).

[17] H. Cercellier, C. Monney, F. Clerc, C. Battaglia, L. Despont, M. G. Garnier, H. Beck, P. Aebi, L. Patthey, H. Berger, and L. Forro, Phys. Rev. Lett. **99**, 146403 (2007).

[18] C. Monney, E. F. Schwier, M. G. Garnier, N. Mariotti, C. Didiot, H. Beck, P. Aebi, H. Cercellier, J. Marcus, C. Battaglia, H. Berger, and A. N. Titov, Phys. Rev. B **81**, 155104 (2010).

[19] C. Monney, C. Battaglia, H. Cercellier, P. Aebi, and H. Beck, Phys. Rev. Lett. **106**, 106404 (2011).

[20] G. Monney, C. Monney, B. Hildebrand, P. Aebi, and H. Beck, Phys. Rev. Lett. **114**, 086402 (2015).

[21] P. Chen, W. W. Pai, Y.-H. Chan, A. Takayama, C.-Z. Xu, A. Karn, S. Hasegawa, M. Y. Chou, S.-K. Mo, A.-V. Fedorov, and T.-C. Chiang, Nat. Commun. **8**, 516 (2018).

[22] M. Kitamura, S. Souma, A. Honma, D. Wakabayashi, H. Tanaka, A. Toyoshima, K. Amemiya, T. Kawakami, K. Sugawara, K. Nakayama, K. Yoshimatsu, H. Kumigashira, T. Sato, and K. Horiba, Rev. Sci. Instrum. **93**, 033906 (2022).

[23] P. Giannozzi, S. Baroni, N. Bonini, M. Calandra, R. Car, C. Cavazzoni, D. Ceresoli, G. L. Chiarotti, M. Cococcioni, I. Dabo, A. D. Corso, S. de Gironcoli, S. Fabris, G. Fratesi, R. Gebauer, U. Gerstmann, C. Gougoussis, A. Kokalj, M. Lazzeri, L. Martin-Samos *et al.*, J. Phys.: Condens. Matter **21**, 395502 (2009).

[24] P. Giannozzi, O. Andreussi, T. Brumme, O. Bunau, M. Buongiorno Nardelli, M. Calandra, R. Car, C. Cavazzoni, D. Ceresoli, M. Cococcioni, N. Colonna, I. Carnimeo, A. Dal Corso, S. de Gironcoli, P. Delugas, R. A. DiStasio Jr, A. Ferretti, A. Floris, G. Fratesi, G. Fugallo, R. Gebauer, U. Gerstmann, F. Giustino *et al.*, J. Phys.: Condens. Matter **29**, 465901 (2017).

[25] J. P. Perdew, K. Burke, and M. Ernzerhof, Phys. Rev. Lett. **77**, 3865 (1996).

[26] See Supplemental Material at http://link.aps.org/supplemental/10.1103/PhysRevMaterials.7.104002 for the folded electron bands in the CDW phase and the CDW-gap opening.

[27] S. Fragkos, R. Sant, C. Alvarez, A. Bosak, P. Tsipas, D. Tsoutsou, H. Okuno, G. Renaud, and A. Dimoloulas, Adv. Mater. Int. **6**, 1801850 (2019).

[28] P. Chen, Y.-H. Chan, X.-Y. Fang, Y. Zhang, M. Y. Chou, S.-K. Mo, Z. Hussain, A.-V. Fedorov, and T.-C. Chiang, Nat. Commun. **6**, 8943 (2015).

[29] M. D. Watson, A. Rajan, T. Antonelli, K. Underwood, I. Marković, F. Mazzola, O. J. Clark, G.-R. Siemann, D. Biswas, A. Hunter, S. Jandura, J. Reichstetter, M. McLaren, P. L. Fèvre, G. Vinai, and P. D. C. King, 2D Mater. **8**, 015004 (2021).

[30] Z. Zhang, H. Zhang, Y. Wu, Z. Zeng, and Z. Hu, Appl. Phys. A **118**, 1043 (2015).

[31] C. Zhang, C. Gong, Y. Nie, K.-A, Min, C. Liang, Y. J. Oh, H. Zhang, W. Wang, S. Hong, L. Colombo, R. M. Wallace, and K. Cho, 2D Mater. **4**, 015026 (2017).

[32] S. Kolekar, M. Bonilla, H. C. Diaz, M. Hashimoto, D. Lu, and M. Batzill, Adv. Quantum Technol. **1**, 1800070 (2018).

[33] T. M. Rice and G. K. Scott, Phys. Rev. Lett. **35**, 120 (1975).

[34] T. Kiss, T. Yokoya, A. Chainani, S. Shin, T. Hanaguri, M. Nohara, and H. Takagi, Nat. Phys. **3**, 720 (2007).

[35] D. W. Shen, Y. Zhang, L. X. Yang, J. Wei, H. W. Ou, J. K. Dong, B. P. Xie, C. He, J. F. Zhao, B. Zhou, M. Arita, K. Shimada, H. Namatame, M. Taniguchi, J. Shi, and D. L. Feng, Phys. Rev. Lett. **101**, 226406 (2008).

[36] H. P. Hughes, J. Phys. C: Solid State Phys. **10**, L319 (1977).

[37] K. Rossnagel, J. Phys.: Condens. Matter **23**, 213001 (2011).

[38] T. Valla, A. V. Fedorov, P. D. Johnson, P.-A. Glans, C. McGuinness, K. E. Smith, E. Y. Andrei, and H. Berger, Phys. Rev. Lett. **92**, 086401 (2004).

[39] F. Zheng and J. Feng, Phys. Rev. B **99**, 161119(R) (2019).

[40] X.-F. Tang, Y.-X. Duan, F.-Y. Wu, S.-Y. Liu, C. Zhang, Y.-Z. Zhao, J.-J. Song, Y. Luo, Q.-Y. Wu, J. He, H. Y. Liu, W. Xu, and J.-Q. Meng, Phys. Rev. B **99**, 125112(R) (2019).